ACS APPLIED ENERGY MATERIALS

www.acsaem.org

Article

Constructing a 2D Heterointerface of $MoS_2/MnIn_2S_4$ with Improved Interfacial Charge Carrier Transfer for Photocatalytic H_2O_2 Production

Uttam Kumar, Emmanuel Picheau, Huanran Li, Zihan Zhang, Takayuki Kikuchi, Indrajit Sinha,* and Renzhi Ma*

Cite This: ACS Appl. Energy Mater. 2025, 8, 3107−3119

Read Online

ACCESS | Metrics & More | Article Recommendations | Supporting Information

ABSTRACT: Photocatalytic oxygen reduction to H_2O_2 is a promising sustainable solar fuel production pathway. Photocatalysts with heterostructure interfaces can suppress charge carrier recombination and endow photogenerated electrons and holes with improved redox potentials. This study develops a heterostructured two-dimensional (2D) $MoS_2/MnIn_2S_4$ photocatalyst for photocatalytic H_2O_2 production. The photocatalyst with an optimal loading of $MnIn_2S_4$ on 2D MoS_2 nanosheets demonstrates the maximum H_2O_2 production rate of 606.7 μmol g^{-1} h^{-1}, approximately 4.2 and 5 times higher than pristine 2D MoS_2 and $MnIn_2S_4$, respectively. The synergistic interaction between 2D MoS_2 nanosheets and $MnIn_2S_4$ results in enhanced charge separation, optical absorption, stability, and recyclability. Reaction pathway studies reveal that H_2O_2 production is through a sequential single-electron O_2 reduction reaction by accumulated photogenerated electrons on the conduction band of the 2D $MoS_2/MnIn_2S_4$ heterostructure. This work presents a noble-metal-free photocatalyst responsive to visible light for solar H_2O_2 generation.

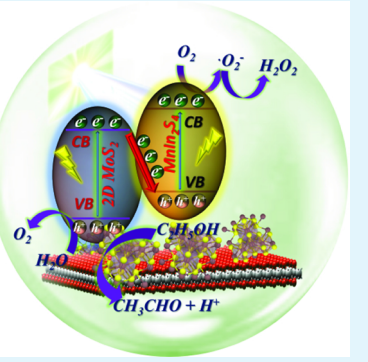

KEYWORDS: *photocatalysis, 2D MoS_2 nanosheets, $MnIn_2S_4$, heterostructures, H_2O_2 production*

1. INTRODUCTION

The rising demand for clean energy has intensified the search for alternatives to conventional energy sources that cause substantial environmental harm.[1,2] Hydrogen peroxide (H_2O_2) is a promising candidate due to its high calorific value, strong oxidation capacity, eco-friendly nature, ease of storage and transportation, and clean decomposition into water and oxygen without producing toxic byproducts.[3,4] These distinctive characteristics make H_2O_2 indispensable in various applications, including medical sterilization, environmental remediation,[5,6] and chemical synthesis.[7] As the demand for H_2O_2 grows, increasing production efficiency is critical to meet its rising need. Currently, the anthraquinone process is the predominant method for large-scale H_2O_2 production. However, this and related methods pose challenges, such as high energy consumption, complexity, and the risk of explosion.[8]

A promising alternative is heterogeneous photocatalysis technology, which harnesses solar energy to produce H_2O_2. This approach is recognized as a green and sustainable process.[9,10] During photocatalysis, H_2O_2 can be generated either through the two-electron ($2e^-$) reduction of O_2 via the catalyst or H_2O oxidation by photogenerated holes.[11] In recent decades, a wide range of photocatalysts have been explored for H_2O_2 production. Notable examples include titanium dioxide (TiO_2)-based photocatalysts,[12] carbon nitride (g-C_3N_4)-based photocatalysts,[13,14] transition metal complexes,[15] transition metal sulfides,[16,17] and bismuth (Bi)-containing semiconductors.[18] Among these, metal sulfides have attracted significant interest in photocatalysis due to their tunable band gaps, favorable electronic structures, and abundant active sites.[19]

In this context, MoS_2, a typical layered transition metal dichalcogenide, has attracted significant attention due to its low cost, large surface area, strong visible light response, tunable bandgap structure, and favorable photocatalytic performance.[20,21] In particular, exfoliated or few-layered MoS_2 nanosheets with a 2D structure have emerged as promising photocatalysts. The unique optical and electronic properties of 2D MoS_2 contribute to better photoresponse and charge separation in photocatalysts.[22] As the number of layers decreases, MoS_2 exhibits enhanced properties that improve its photocatalytic performance.[23,24] To date, several studies have reported significant enhancements in photocatalytic activity using few-layer MoS_2 heterojunction composites, including In_2S_3/MoS_2,[25] CdS/MoS_2,[26] MoS_2/rGO/CdS,[27] WS_2−

Received: December 22, 2024
Revised: February 12, 2025
Accepted: February 17, 2025
Published: February 24, 2025

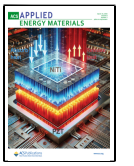

Scheme 1. Schematic Diagram Illustrating the Synthesis Process of As-Designed MS/MnIS-*x* Heterostructure Photocatalysts

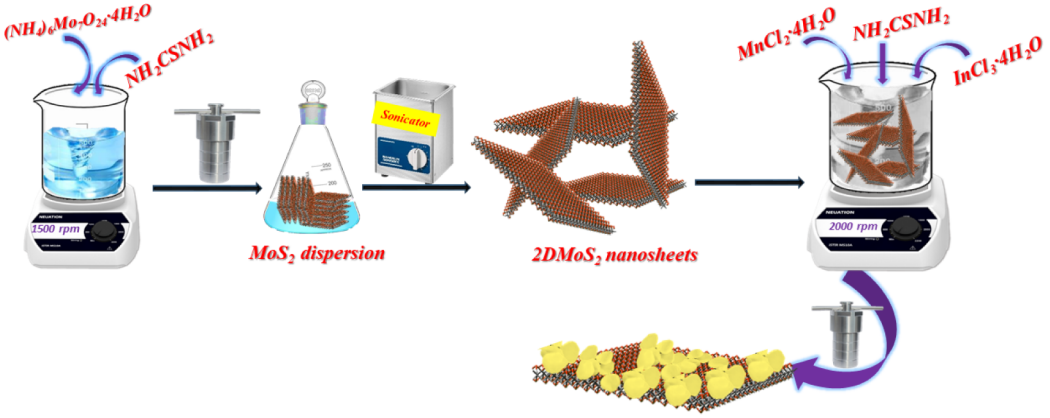

MoS_2,[28] MoS_2/g-C_3N_4,[29] and $MoS_2/Mn_{0.2}Cd_{0.8}S$.[30] These heterostructured photocatalysts, which couple 2D MoS_2 with other semiconductors, facilitate enhanced separation of photogenerated charge carriers and broaden solar light absorption. Composite formation effectively suppresses the recombination of charge carriers, thereby improving overall photocatalytic efficiency.

On the other hand, ternary chalcogenide AB_2X_4 semiconductors have recently been recognized for their significant potential as visible-light-active photocatalysts, owing to their tunable optical properties, unique electronic structure, narrow band gaps, and chemical photostability.[31,32] Among them, $MnIn_2S_4$ stands out as an ideal photocatalyst due to its appropriate band gap for visible light absorption and the high reduction potential of its conduction band electrons. Chen et al. recently developed 2D/2D g-C_3N_4/$MnIn_2S_4$ Z-scheme heterostructured photocatalysts for H_2 production and antibiotic degradation. Their study showed that heterostructure formation significantly enhanced visible light absorption and promoted efficient interfacial charge separation, resulting in superior photocatalytic performance compared to pristine g-C_3N_4 and $MnIn_2S_4$.[33] Similarly, Song et al. fabricated Cu_7S_4/$MnIn_2S_4$ semiconductor heterostructures using a simple oil bath and hydrothermal method. The nanocomposite, featuring ultrathin 2D nanosheets and Cu_7S_4 nanoparticles uniformly distributed on $MnIn_2S_4$, exhibited a photocatalytic hydrogen evolution rate of 13.81 μmol h^{-1}, nearly 18 times higher than pure $MnIn_2S_4$. The enhanced performance was attributed to the forming of a p-n heterojunction that suppressed electron−hole recombination.[34] Deng et al. designed and constructed a $MnIn_2S_4/WO_3$ (Yb, Tm) photocatalytic system, incorporating a Z-scheme heterojunction to regulate spatial charge separation and improve light absorption through Yb^{3+} and Tm^{3+} doping. The system was evaluated for H_2O_2 production, showing remarkable activity, producing 37.2 and 8.8 times more H_2O_2 than WO_3 and $MnIn_2S_4$, respectively.[35] However, there are no prior reports on the development of a 2D/2D $MoS_2/MnIn_2S_4$ heterostructure photocatalyst.

In the current study, a heterostructure was constructed by combining few-layered MoS_2 with $MnIn_2S_4$, effectively integrating the advantages of both materials. This combination exhibits strong visible-light absorption, a low recombination rate of photoinduced electron−hole pairs, and excellent photocatalytic activity. Herein, we design a novel 2D MoS_2/$MnIn_2S_4$ heterostructure photocatalyst that was successfully fabricated through a green hydrothermal process. As illustrated in Scheme 1, small petals of $MnIn_2S_4$ were embedded onto ultrathin 2D MoS_2 nanosheets, forming a well-integrated heterostructure. The 2D morphology of both $MnIn_2S_4$ and MoS_2 enhances interfacial contact and facilitates efficient charge transfer between the two components. Various characterization techniques, including X-ray diffractometer (XRD), scanning electron microscope (SEM), transmission electron microscope (TEM), diffuse reflectance spectroscopy (DRS), photoluminescence (PL), contact angle, and electrochemical measurements, were employed to investigate the intrinsic relationship between the 2D heterointerface structure and the significantly enhanced photocatalytic activity of the $MoS_2/MnIn_2S_4$ heterostructure. The photocatalytic activities of the resulting samples were assessed through the H_2O_2 production. The improved photocatalytic performance of the heterostructure systems can primarily be attributed to the Z-scheme mechanism. This mechanism effectively harnesses the strong reduction capability of photogenerated electrons in the conduction band of $MnIn_2S_4$ nanosheets and the high oxidation capability of photogenerated holes in the valence band of 2D MoS_2 nanosheets. Furthermore, the mechanism of the H_2O_2 production process has been thoroughly investigated. The pathway is elucidated through scavenger studies, and the reactive species involved in the photocatalytic H_2O_2 production are identified based on confirmatory tests. Our research will guide the future design of more versatile Z-scheme sulfide/chalcogenide heterostructure composites for H_2O_2 production.

2. EXPERIMENTAL SECTION

2.1. Materials. Ammonium molybdate tetrahydrate ($(NH_4)_6Mo_7O_{24}{\cdot}4H_2O$), indium chloride tetrahydrate ($InCl_3{\cdot}4H_2O$), ethylenediaminetetraacetic acid disodium (EDTA-2Na), *para*-benzoquinone (*p*-BQ). Thiourea (NH_2CSNH_2), silver nitrate ($AgNO_3$), manganese chloride tetrahydrate ($MnCl_2{\cdot}4H_2O$), and nitro blue tetrazolium (NBT) were purchased from Wako Chemicals. All reagents were used as received without any further purification.

2.2. Preparation of 2D MoS_2 Nanosheets. Pristine MoS_2 nanosheets were prepared through a one-step hydrothermal treatment.[36] Typically, 1 mmol of $(NH_4)_6Mo_7O_{24}{\cdot}4H_2O$ and 30 mmol of NH_2CSNH_2 were dissolved in 35 mL of deionized water under vigorous stirring to form a homogeneous solution. The resulting mixture was then transferred to a 50 mL Teflon-lined autoclave and maintained at 210 °C for 24 h. After the reaction, the precipitates were allowed to cool

https://doi.org/10.1021/acsaem.4c03296
ACS Appl. Energy Mater. 2025, 8, 3107−3119

naturally to room temperature, washed multiple times with water and absolute ethanol, and collected by ultracentrifugation at 25,000 rpm. The final products were dried at 60 °C in a vacuum oven and stored for further use.

For the preparation of 2D MoS_2 nanosheets, 150 mg of the synthesized MoS_2 powder was initially dispersed in 80 mL of a mixed solvent of *N*-methyl pyrrolidone (NMP) and deionized water (50/50 (vol%)) in a stoppered conical flask.[23] The flask was then subjected to ultrasonic bath sonication for 120 min. The resulting suspension was left overnight, and the dispersion of exfoliated MoS_2 was isolated. Finally, the exfoliated MoS_2 was centrifuged at 25,000 rpm for 25 min, and the exfoliated MoS_2 powder was collected for further use.

2.3. Preparation of $MnIn_2S_4$. First, 0.198 g of Manganese chloride tetrahydrate (1 mmol) and 0.537 g of indium chloride tetrahydrate (2 mmol) were dissolved in 35 mL of deionized water under vigorous stirring for 1 h. Then, 0.381 g of thiourea (5 mmol) was added to the solution and stirred for two more hours. The suspension was transferred to a Teflon-lined stainless steel autoclave and heated at 210 °C for 24 h. Once the reaction was complete, the samples were allowed to cool naturally to room temperature, washed with ethanol, and dried in a vacuum oven.[33]

2.4. Synthesis of 2D $MoS_2/MnIn_2S_4$. The 2D $MoS_2/MnIn_2S_4$ heterostructures with varying concentrations of $MnIn_2S_4$ nanosheets were synthesized using a straightforward hydrothermal method. Initially, a certain amount of 2D MoS_2 nanosheets was dispersed in deionized water and subjected to ultrasonication for 60 min to form a uniform suspension. Next, manganese chloride tetrahydrate (1 mmol), indium chloride tetrahydrate (2 mmol), and thiourea (5 mmol) were dissolved in deionized water with constant stirring on a magnetic stirrer. After 1 h of stirring, the 2D MoS_2 suspension was added to the mixture and stirred for an additional 2 h. The resulting mixture was then transferred to a Teflon-lined autoclave and heated at 210 °C for 24 h. Once the reaction was complete, the samples were allowed to cool naturally to room temperature, then washed multiple times with water and ethanol and collected by centrifugation. The process produced 2D $MoS_2/MnIn_2S_4$ nanocomposites with varying $MnIn_2S_4$ weight ratios, designated as MS/MnIS-*x*, where *x* corresponds to 10, 20, 40, 60, and 80, representing the weight percent of $MnIn_2S_4$ relative to 2D MoS_2 in the reaction system.

2.5. Photocatalytic H_2O_2 Production. The photocatalytic H_2O_2 production experiment was carried out by dispersing 5 mg of the synthesized photocatalyst powder in 20 mL of a deionized water/ethanol mixture (95:5 vol%). The dispersion was facilitated through 10 min of ultrasonic bath treatment. Afterward, oxygen was bubbled through the solution and kept in the dark for 30 min to ensure equilibrium. The suspension was then exposed to irradiation from a solar simulator. Following 1 h of photocatalytic reaction, a 2 mL aliquot was extracted, and the photocatalyst was separated from the reaction solution.

The concentration of H_2O_2 was quantified using the iodometric method.[37−39] To the 2 mL aliquot (post photocatalyst removal), 2 mL of 0.1 M KI and 50 μL of 0.01 M ($(NH_4)_6Mo_7O_{24}\cdot 4H_2O$) were added and thoroughly mixed. The reaction mixture was kept in the dark for 20 min to allow for a complete reaction. In this process, KI is oxidized by H_2O_2, releasing I_2, which then reacts with excess I^- (from KI) to form the yellow-colored triiodide anion (I_3^-) through the reaction: $H_2O_2 + 3I^- + 2H^+ \rightarrow I_3^-$. The amount of I_3^- generated is directly proportional to the concentration of H_2O_2 present in the sample. Finally, the absorbance of the resulting solution was measured using UV−vis spectroscopy, showing a characteristic intense absorption peak around 352 nm.

Furthermore, to achieve optimal yields in H_2O_2 production, the experimental conditions, including pH, were systematically optimized. The primary reactive species generated during the photocatalytic process were identified using trapping experiments under irradiation. The contributions of electrons (e^-), superoxide radicals ($\bullet O_2^-$), and holes (h^+) to H_2O_2 production were assessed by introducing $AgNO_3$, p-BQ, and EDTA-2Na as scavengers.

3. CHARACTERIZATION METHODS

Crystalline phases were characterized by powder XRD using Cu Kα radiation (Ultima IV, Rigaku, Japan) with a step size of 0.01° and scan rate of 1°/min, covering a 2θ range from 5° to 80°. The morphology and elemental mapping were analyzed using an SEM (JEOL, JSM-6010LA) and TEM/STEM (JEOL-3100). The UV−vis diffuse reflectance spectrum was obtained using a solid state spectrophotometer (SolidSpec-3700 DUV, Shimadzu, Japan), equipped with an integrating sphere assembly, using $BaSO_4$ as a reflectance reference sample. Similarly, a UV−vis spectrophotometer (U-4100 Hitachi) was used to measure the absorbance of the liquid sample. The photoexcited charge carrier separation of as-prepared photocatalysts was analyzed using a fluorescence spectrophotometer (F-7000, Hitachi). Water/ethanol adsorption properties were examined using the contact angle instruments (Model, CA, XP).

3.1. Electrochemical Measurements Tests. The electrochemical studies, specifically Mott−Schottky (MS) and electrochemical impedance spectroscopy (EIS), were conducted using a standard three-electrode setup in an electrochemical workstation (CHI-760E). A carbon electrode was employed as the counter electrode, an Ag/AgCl electrode served as the reference electrode, and carbon paper was used as the working electrode. The working electrode was prepared as follows: 2.5 mg of the photocatalyst was dispersed in 250 μL of a deionized water/ethanol mixture (1:1 ratio) via 30 min of ultrasonic bath sonication. Then, 10 μL of Nafion reagent was added, and the mixture was sonicated for an additional 30 min. Afterward, 40 μL of the resulting suspension was evenly applied to the carbon paper within a 0.5 cm^2 area and allowed to dry at room temperature to form the working electrode. Note that 0.5 M Na_2SO_4 electrolyte was used for the above measurements (the pH value of the electrolyte was around 7). The band potential of the photocatalysts was determined by fitting the MS plots. The potentials obtained against Ag/AgCl (reference electrode) were then converted to the normal hydrogen electrode (NHE) scale using eq 1. The photoelectrode was fabricated using the same protocol for the photocurrent measurement. A solar simulator was used as the light source to illuminate the electrode.

$$V_{NHE} = V_{(Ag/AgCl)} + 0.059 \times pH + 0.197 \quad (1)$$

4. RESULTS AND DISCUSSION

Powder XRD was carried out to investigate the phase purity and crystal structures of the 2D MoS_2, $MnIn_2S_4$, and MS/MnIS-*x* heterostructures. Figure 1 shows the corresponding XRD patterns of the various samples. The XRD pattern traced

https://doi.org/10.1021/acsaem.4c03296
ACS Appl. Energy Mater. 2025, 8, 3107−3119

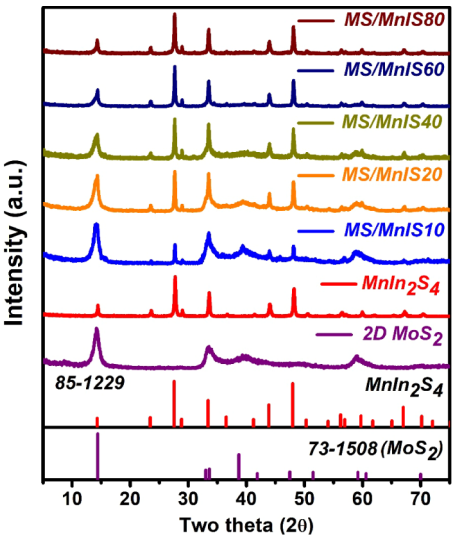

Figure 1. XRD patterns of 2D MoS_2, $MnIn_2S_4$, and MS/MnIS-*x* heterostructure photocatalysts.

in purple is of the as-prepared 2D MoS_2 nanosheets. The observed diffraction peaks at two theta (2θ) values of 14.2°, 33.4°, and 58.8° can be uniquely attributed to the (002), (100), and (110) crystal planes of standard hexagonal MoS_2 (2H MoS_2, JCPDS card No. 731508), respectively, revealing the high purity of the sample. There is an apparent broadening of all the peaks in the diffraction patterns, which suggests the nanoscales of the crystallites in different dimensions.[36] The red trace represents the diffraction pattern of standard cubic structure $MnIn_2S_4$ phase (JCPDS No. 85-1229). The characteristic peaks of MoS_2 at (002) and (110) were observed in all 2D $MoS_2/MnIn_2S_4$ heterostructures, confirming that the composite structure consists of hexagonal MoS_2 and cubic $MnIn_2S_4$. No diffraction peaks associated with impurities were detected, confirming the high purity of the synthesized heterostructure photocatalysts.

The optical properties of the 2D MoS_2 nanosheets, produced via liquid-phase ultrasonication, were examined using UV−visible absorbance spectrophotometry. A slight shift in the UV−visible spectral peak toward a lower wavelength (Figure S1a) suggests a change in the bandgap due to exfoliation. Additionally, the light absorbance in the visible region was significantly enhanced after exfoliation compared to bulk MoS_2. Figure S1b indicates the successful and stable dispersion of exfoliated MoS_2 nanosheets.

Similarly, the optical characteristics of 2D MoS_2, $MnIn_2S_4$, and the MS/MnIS-*x* heterostructure were explored through solid-state UV−Vis NIR analysis, as shown in Figure 2. From the absorbance spectra, it is clear that 2D MoS_2 shows a strong visible light absorption band at a range of 300−1350 nm. Similarly, pristine $MnIn_2S_4$ exhibited visible light absorption with a characteristic absorption edge near 680 nm. Compared to pristine $MnIn_2S_4$, the formation of the MS/MnIS-*x* heterostructure resulted in a significant redshift of the absorption edge, with strong absorption observed in the visible to NIR range from approximately 340 to 1350 nm. The DRS results demonstrated that the formation of 2D $MoS_2/MnIn_2S_4$ heterostructures allows for more efficient exploitation of solar energy. Further, the band gap energy (E_g) of the 2D MoS_2, $MnIn_2S_4$, was calculated using Tauc's plot using eq 2.

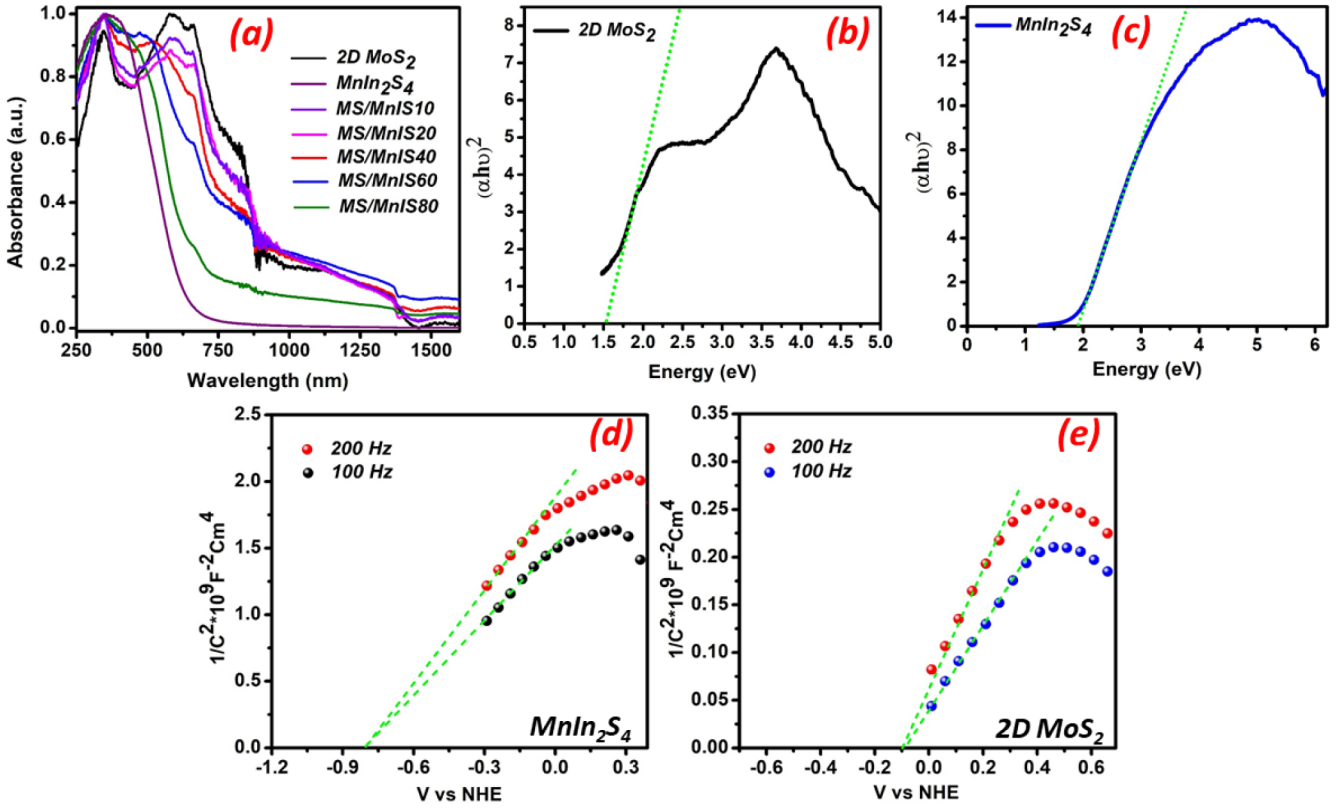

Figure 2. (a) Solid-state UV-DRS absorbance spectra of 2D MoS_2, $MnIn_2S_4$, and MS/MnIS-*x* heterostructure photocatalysts. (b,c) Tauc plot of 2D MoS_2 and $MnIn_2S_4$. Mott−Schottky plot of (d) $MnIn_2S_4$ and (e) 2D MoS_2.

https://doi.org/10.1021/acsaem.4c03296
ACS Appl. Energy Mater. 2025, 8, 3107−3119

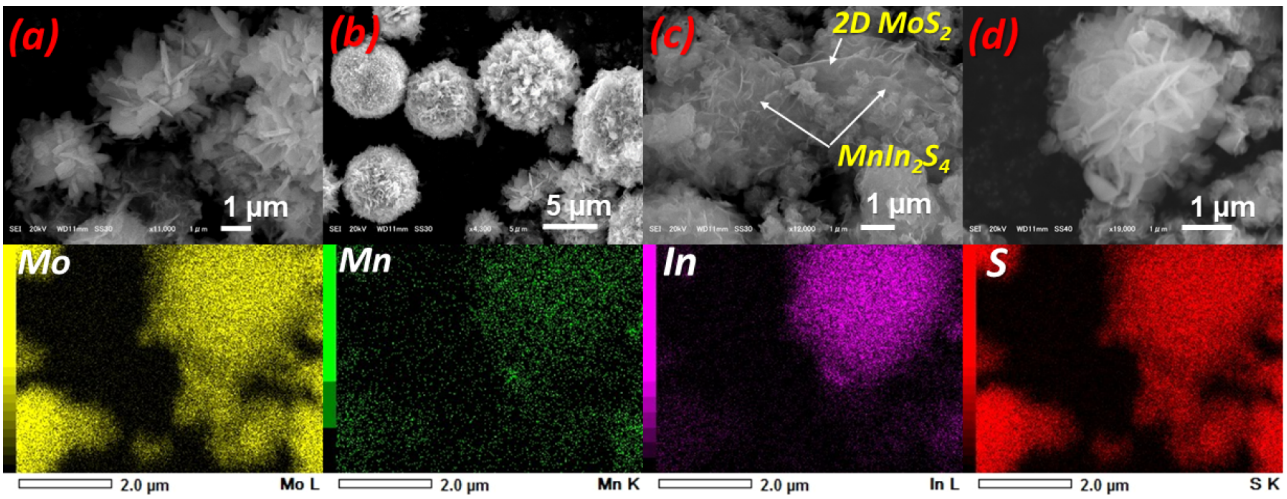

Figure 3. (a,b) SEM images of pristine $MnIn_2S_4$. (c) SEM images of MS/MnIS40 heterostructure photocatalysts. (d) SEM image with corresponding elemental maps (Mo, Mn, In, S) of MS/MnIS40 heterostructure photocatalysts.

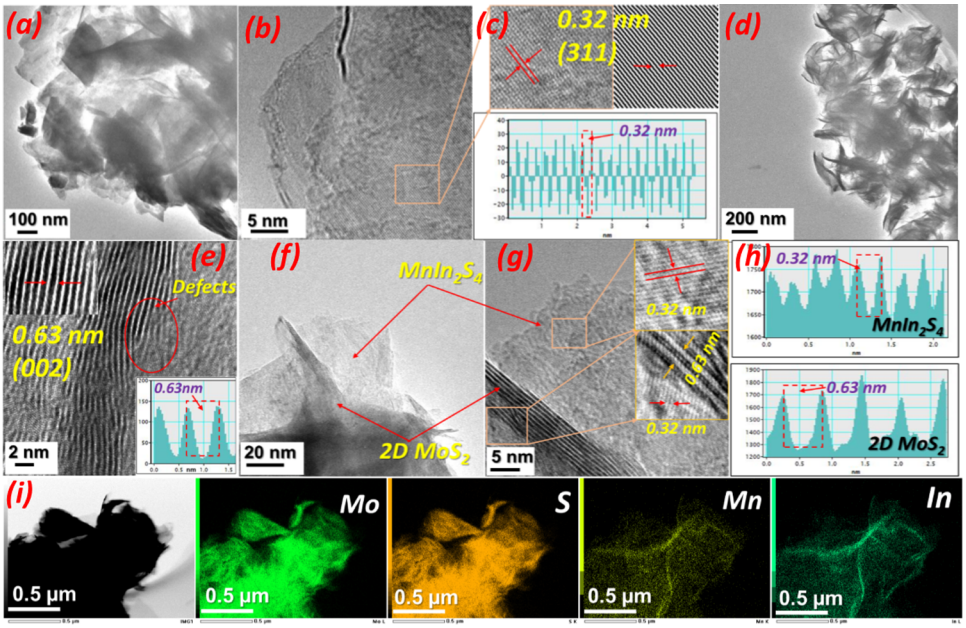

Figure 4. TEM, HR-TEM, and IFFT images of (a–c) pure $MnIn_2S_4$, (d,e) 2D MoS_2, (f–h) MS/MnIS40 heterostructure. (i) STEM elemental mapping of MS/MnIS40 heterostructure photocatalysts.

$$(\alpha hv)^{1/n} = A(hv - E_g) \quad (2)$$

Where hv and α represent the photoelectron energy and absorption coefficient, respectively. The measured band gap energies of 2D MoS_2 and $MnIn_2S_4$ were 1.52 and 1.88 eV, respectively, as shown in Figure 2b,c. The calculated band gap of bulk MoS_2 (before exfoliation) is provided in Figure S2a. These results indicate that, after successful exfoliation into nanosheets, the band gap energy increased from 1.31 to 1.52 eV. Furthermore, the Tauc plots of MS/MnIS-x photocatalysts are provided in Figure S2b–f.

Mott–Schottky (MS) measurements were carried out at 100 and 200 Hz to investigate the band structure and semiconductor type. Figure 2d,e shows the MS curves for 2D MoS_2 and $MnIn_2S_4$ samples. Both 2D MoS_2 and $MnIn_2S_4$ exhibited positive MS slopes, confirming their n-type semiconductor characteristics. The conduction band potentials were determined to be −0.1 V for 2D MoS_2 and −0.81 V for $MnIn_2S_4$ versus NHE by fitting the $1/C^2$ vs potential plot. By combining the MS results with the energy band gaps of 2D MoS_2 and $MnIn_2S_4$, as determined by the Tauc plot, the valence band positions were calculated to be 1.42 V for 2D MoS_2 and 1.07 V for $MnIn_2S_4$, respectively, using the formula $E_{VB} = E_{CB} + E_g$.[40,41] Here, E_{VB} represents the valence band edge position, and E_{CB} denotes the conduction band edge position. It is noteworthy that the CB potentials of $MnIn_2S_4$ are more negative than the reduction potentials of $O_2/\bullet O_2^-$ (−0.33 V vs NHE) and O_2/H_2O_2 (0.68 V vs NHE). This indicates that their reduction potentials are sufficient to drive the formation of H_2O_2.

The morphologies and microstructures of $MnIn_2S_4$, 2D MoS_2, and the MS/MnIS40 heterostructures were thoroughly characterized using SEM and TEM. The analysis revealed that both 2D MoS_2 and $MnIn_2S_4$ exhibit a layered structure with

https://doi.org/10.1021/acsaem.4c03296
ACS Appl. Energy Mater. 2025, 8, 3107–3119

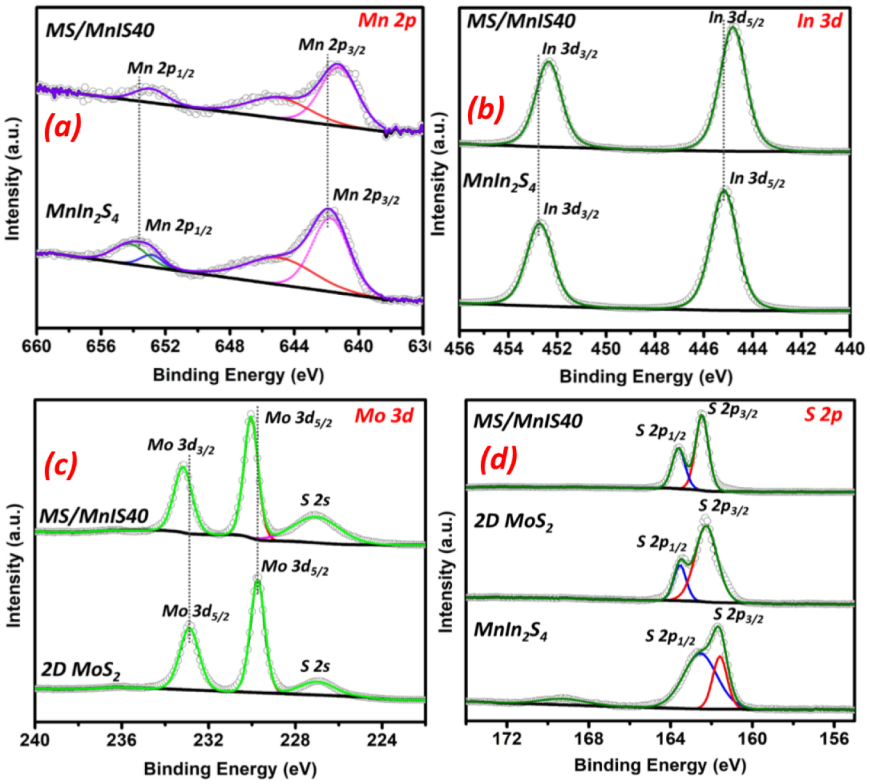

Figure 5. XPS spectra of 2D MoS_2, $MnIn_2S_4$, and MS/MnIS40: (a) Mn 2p, (b) In 3d, (c) Mo 3d, and (d) S 2p.

lateral dimensions of several hundred nanometers, respectively. Figure 3 presents the SEM images of $MnIn_2S_4$ and the MS/MnIS40. The pure $MnIn_2S_4$ exhibits a distinctive nanoflower-like structure composed of small petal-like features, as shown in Figure 3a,b. Notably, these petal-like formations gradually orient themselves into a cohesive nanoflower morphology. This unique morphology is advantageous for photocatalytic H_2O_2 production, as it provides many active sites for the reaction. Figure S3 displays the SEM elemental mapping images of pristine $MnIn_2S_4$ photocatalysts, revealing the homogeneous distribution of Mn, In, and S elements in pure $MnIn_2S_4$. Similarly, the SEM images of the MS/MnIS40 heterostructure (Figure 3c,d) illustrate the formation of small petal-like nanostructures of $MnIn_2S_4$ embedded on the thin, layered 2D MoS_2 nanosheets. The corresponding SEM elemental mapping images confirm the uniform distribution of Mn, In, Mo, and S elements within the MS/MnIS40 heterostructure, indicating partial coverage of the 2D MoS_2 surface by $MnIn_2S_4$. However, as the $MnIn_2S_4$ loading increases, excessive deposition leads to agglomeration, resulting in the formation of nanoflowers that entirely cover the 2D MoS_2 surface. Additionally, Figure S4a,b presents the SEM images and elemental mapping for the MS/MnIS60 and MS/MnIS80 samples. No extra elements are detected in these samples, confirming the high purity and successful formation of the heterostructure in the synthesized materials.

To further confirm the morphology and structure of 2D MoS_2, $MnIn_2S_4$, and the MS/MnIS40 heterostructure were observed using TEM and high-resolution TEM (HRTEM).

Notably, the TEM images of the $MnIn_2S_4$ (Figure 4a) and 2D MoS_2 (Figure 4d) display layered structures with a nearly transparent appearance, consistent with the presence of ultrathin nanosheets. The inverse fast Fourier transform (IFFT) images and spectra of the HRTEM images of pristine $MnIn_2S_4$, as shown in Figure 4c, reveal distinct lattice fringes of 0.32 nm, corresponding to the (311) crystal plane of $MnIn_2S_4$, which is consistent with the intense peak observed in the XRD pattern (JCPDS No. 85-1229). Figure 4d reveals that the 2D MoS_2 consists of a few-layered, curled nanosheets with a scattered orientation. As shown in Figure 4e, the interlayer spacing of 6.3 Å corresponds to the (002) planes of MoS_2, verifying its hexagonal (2H) structure. These nanosheets exhibit higher crystallinity and a relatively intact layered configuration, which aligns well with the XRD results. The HRTEM images of the 2D MoS_2 nanosheets in Figures 4e and S5a reveal structural defects in the 2H MoS_2, typically characterized by cracks and misaligned basal planes, as previously reported in the literature.[36,42] After forming the 2D MoS_2 and $MnIn_2S_4$ heterostructures (MS/MnIS40), the structure exhibits an ultrathin nanosheet-on-nanosheet morphology (Figure 4f,g) with a large contact surface. The IFFT images and spectra derived from the HRTEM image of the 2D/2D heterostructure (Figure 4h) reveal lattice fringes of $MnIn_2S_4$ (0.32 nm) and 2D MoS_2 (0.63 nm), confirming strong interfacial contact between the two materials and the successful formation of the heterostructure. This extensive, intimate interface enables multiple pathways for carrier migration, enhancing charge separation efficiency. Furthermore, the elemental mapping analysis of the selected region in Figure S5b for the MS/MnIS40 heterostructure clearly demonstrates the well-defined spatial distribution of Mo, Mn, In, and S (Figure 4i). The electron microscopy results clearly reveal a uniform and intimate coupling within the 2D structure of $MoS_2/MnIn_2S_4$, which substantially increases the contact area. This expanded interface improves the separation of photoinduced charge carriers and facilitates more efficient

https://doi.org/10.1021/acsaem.4c03296
ACS Appl. Energy Mater. 2025, 8, 3107−3119

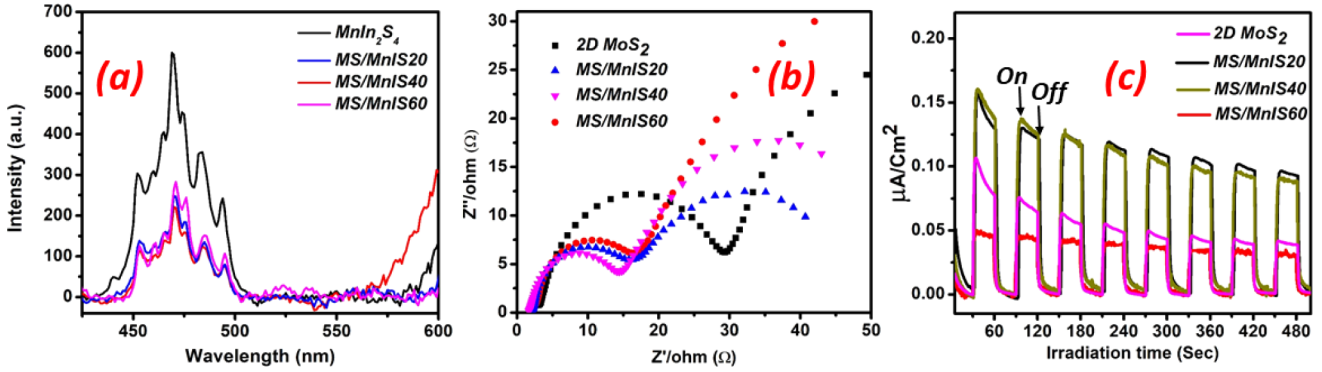

Figure 6. (a) PL spectra of $MnIn_2S_4$ and MS/MnIS-*x* heterostructure photocatalysts; (b,c) Nyquist plot and photocurrent studies of 2D MoS_2 and MS/MnIS-*x* heterostructure photocatalysts.

electron transfer within the heterostructure, leading to a significant enhancement in photocatalytic activity.[43]

The X-ray photoelectron spectroscopy (XPS) analysis revealed the interfacial chemical states and interactions in the 2D MoS_2, $MnIn_2S_4$, and MS/MnIS40 samples. The HR-XPS data was calibrated using a C 1s binding energy of 284.8 eV.[44] The XPS survey spectrum in Figure S6 confirms the presence of Mo and S elements in MoS_2 and Mn, In, and S elements in $MnIn_2S_4$. Similarly, the survey spectrum of the MS/MnIS40 samples shows Mo, Mn, In, and S, further indicating the successful formation of heterostructures of 2D MoS_2 and $MnIn_2S_4$. The high resolution (HR) Mn 2p spectra of $MnIn_2S_4$ (Figure 5a) show characteristic peaks at binding energies of 641.8 and 645.3 eV for Mn $2p_3/_2$ and at 652.8 and 654.1 eV for Mn $2p_1/_2$. These peaks are attributed to the Mn^{2+} and Mn^{4+} oxidation states.[35] In the Mn 2p spectra of the MS/MnIS40 heterostructure (Figure 5a), the Mn $2p_3/_2$ and Mn $2p_1/_2$ peaks are slightly shifted toward lower binding energies. Figure 5b shows the In 3d spectra for both $MnIn_2S_4$ and MS/MnIS40, where the binding energies of the In 3d peaks at 445.1 eV (In $3d_5/_2$) and 452.7 eV (In $3d_3/_2$) confirm the +3 oxidation state of In in $MnIn_2S_4$. Compared to pure $MnIn_2S_4$, the In 3d XPS peaks in the MS/MnIS40 heterostructures also shift toward lower binding energies.

The Mo 3d spectrum (Figure 5c) exhibits two distinct peaks at 229.7 and 232.9 eV, corresponding to the binding energies of Mo $3d_{5/2}$ and Mo $3d_{3/2}$, associated with the 2H phase of MoS_2. These findings confirm that Mo in MoS_2 is in the +4 oxidation state. An additional peak observed at a binding energy of 226.8 eV corresponds to the S 2s state, indicating the interaction between S and Mo. Compared to 2D MoS_2, the characteristic Mo 3d peaks of MS/MnIS40 shift slightly to higher binding energies. Conversely, the Mn 2p and In 3d peaks in $MnIn_2S_4$ shift to lower binding energies upon forming MS/MnIS40 heterostructure, suggesting a strong interaction between 2D MoS_2 and $MnIn_2S_4$.[45] A shift to lower binding energy indicates an increase in electron cloud density, while a shift to higher binding energy implies a decrease in electron cloud density. Consequently, the binding energy shifts observed in the XPS reveal the direction of electron transfer from 2D MoS_2 to $MnIn_2S_4$ in the MS/MnIS40 heterostructure system.[46−49]

Figure 5d displays the HR S 2p spectra of $MnIn_2S_4$, 2D MoS_2, and MS/MnIS40 heterostructure. The S 2p spectrum displays two distinct peaks at 162.2 eV for S $2p_{3/2}$ and 163.5 eV for S $2p_{1/2}$, corresponding to the binding energies of S^{2-} ions in MoS_2.[50] The S 2p binding energies of $MnIn_2S_4$ were detected at 161.6 eV for S $2p_{3/2}$ and 162.5 eV for S $2p_{1/2}$, respectively. The small peak at a binding energy of 168.9 eV is attributed to sulfate species formed by the oxidation of sulfur in air.[51]

A photoluminescence (PL) study of the photocatalytic material reveals insights into photoinduced charge carriers' migration, transfer, and separation efficiency. Typically, a decrease in the PL emission intensity corresponds to a reduction in the charge carrier recombination rate, indicating enhanced separation of photogenerated electron−hole pairs.[38] The PL emission spectra of pristine $MnIn_2S_4$ and MS/MnIS-*x*, excited at 340 nm at room temperature, are shown in Figure 6a. The PL spectra of MS/MnIS10 and MS/MnIS80 are provided in Figure S7a. A prominent emission peak centered at 450 nm is observed for the as-prepared photocatalysts. In contrast, the MS/MnIS40 heterostructure exhibits the lowest PL intensity among the other photocatalysts. This suggests that incorporating 40% $MnIn_2S_4$ onto 2D MoS_2 enhances the separation of electron−hole pairs on the catalyst's surface. This enhancement likely contributes to the superior photocatalytic performance of the MS/MnIS40 heterostructure toward the oxygen reduction reaction (ORR). The primary reason is the reduced recombination rate of photogenerated electrons, which allows them to migrate efficiently to the surface of $MnIn_2S_4$, thereby enhancing the photoreduction process. Furthermore, electrochemical impedance spectroscopy (EIS) was conducted to assess the interfacial charge transfer behavior of the prepared photocatalysts. Figure 6b presents the Nyquist plots of the 2D MoS_2 and MS/MnIS-*x* heterostructure systems. Figure S7b shows the Nyquist plot of $MnIn_2S_4$, MS/MnIS10, and MS/MnIS80 photocatalysts. As illustrated, the MS/MnIS40 system exhibits the smallest arc diameter, signifying reduced charge transfer resistance and impedance, suggesting improved charge migration.[52] In the MS/MnIS40 heterojunction, the heterostructure formation is well-balanced with a proper interface, ensuring effective electron transport from 2D MoS_2 to $MnIn_2S_4$ while minimizing charge recombination. In contrast, lower $MnIn_2S_4$ loadings (10 and 20 wt%) result in insufficient heterojunction formation, leading to higher recombination losses. On the other hand, excessive $MnIn_2S_4$ content (60 and 80 wt%) causes nanosheet agglomeration, which not only covers the active sites on the 2D MoS_2 surface but also leads to charge accumulation, ultimately increasing resistance. Figure S7d presents the corresponding fitting circuit along with the R*s* and R*ct* values for 2D MoS_2, $MnIn_2S_4$, and MS/MnIS-*x* heterostructure photocatalysts. Similar results were observed for these

https://doi.org/10.1021/acsaem.4c03296
ACS Appl. Energy Mater. 2025, 8, 3107−3119

materials in the transient photocurrent responses (Figure 6c). The charge separation process is reflected in the transient photocurrent, as shown by the chronoamperometry. A significant spike in current occurs immediately upon light exposure, followed by a rapid decline when the light is turned off (Figure 6c). Notably, the MS/MnIS40 heterostructure photocatalyst exhibits a significantly higher photocurrent density compared to the other prepared photocatalysts. The photocurrent response of $MnIn_2S_4$, MS/MnIS10, and MS/MnIS80 are given in Figure S7c. The combined observations from PL, EIS, and photocurrent experiments clearly demonstrate that the MS/MnIS40 heterostructure can serve as an efficient photocatalyst, exhibiting enhanced photocatalytic H_2O_2 production.

To investigate the impact of photocatalyst surface properties on its activity, we performed contact angle measurements to assess the hydrophilic characteristics of photocatalysts. These experiments were carried out under similar conditions, as a reactant of 5% (vol) ethanol-containing water was used. After 2 s of contact with water/ethanol mixture droplets, the contact angle of 2D MoS_2, $MnIn_2S_4$ (Figure S8), MS/MnIS10, MS/MnIS20, MS/MnIS40, MS/MnIS60, and MS/MnIS80 are 43.4°, 14.9°, 37.4°, 30.5°, 23.9°, 20.5 ° and 18.1°; results confirmed its hydrophilic nature (Figure 7). A smaller contact

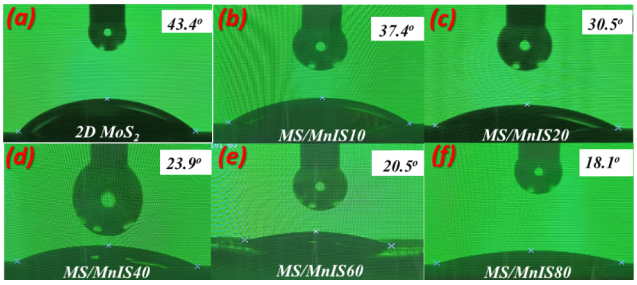

Figure 7. Contact angle results: (a) 2D MoS_2, (b) MS/MnIS10, (c) MS/MnIS20, (d) MS/MnIS40, (e) MS/MnIS60, and (f) MS/MnIS80.

angle signifies better wetting of the photocatalyst particle surface by the solvent molecules. It also implies longer residence times for solvent molecules from the water/ethanol mixture, facilitating better contact between the photocatalyst particles and reactants.[53] Additionally, the hydrophilic surface improves the uniform dispersion of the photocatalyst within the reaction system, leading to increased reaction rates and selectivity.

4.1. Photocatalytic H_2O_2 Production. The photocatalytic activities of 2D MoS_2, $MnIn_2S_4$, and MS/MnIS-*x* for H_2O_2 production were evaluated under various controlled conditions at room temperature and atmospheric pressure. Initially, H_2O_2 production was tested without a catalyst or light irradiation. Under these conditions, no H_2O_2 was detected, confirming that the H_2O_2 production reaction at room temperature is driven by solar light in the presence of photocatalysts. Figure S9a illustrates the H_2O_2 production rates for different photocatalysts in O_2-bubbled water at pH 3. The MS/MnIS-*x* heterostructure photocatalysts demonstrated significant H_2O_2 formation compared to pristine 2D MoS_2 and $MnIn_2S_4$. Among the various $MnIn_2S_4$ loadings, the 40 wt% loading onto 2D MoS_2 achieved a remarkable H_2O_2 production rate of 240.2 μmol g^{-1} h^{-1}. However, further increasing the $MnIn_2S_4$ loading onto the 2D MoS_2 resulted in a decline in H_2O_2 production, likely due to excessive 2D MoS_2 active surface coverage. Moreover, the excess loading caused agglomeration of the nanosheets, as confirmed by the SEM image and elemental mapping of MS/MnIS60 and MS/MnIS80 in Figure S4a,b. This excessive coverage impairs visible light absorption and hinders efficient interfacial charge transfer, as evidenced by the EIS and PL results.

In contrast, when ethanol was introduced into the reaction mixture as a sacrificial agent, the photocatalytic H_2O_2 production rate was improved, as shown in Figure S9a. Figure 8a displays the time-dependent curve of photocatalytic H_2O_2 production of different photocatalysts. This enhancement confirms the oxidation of ethanol by the photogenerated holes. The best-performing photocatalyst, MS/MnIS40, achieved an impressive H_2O_2 production rate of 606.7 μmol g^{-1} h^{-1}, whereas pristine 2D MoS_2 and $MnIn_2S_4$ exhibited only 147.4 μmol g^{-1} h^{-1} and 121.5 μmol g^{-1} h^{-1}, respectively. This corresponds to an approximately 4.2-fold increase compared to pristine 2D MoS_2 and a 5-fold increase compared to $MnIn_2S_4$ alone. Notably, the H_2O_2 generation rate of our MS/MnIS40 surpassed that of recently reported heterostructure-based photocatalysts (Figure 8h and Table S1).

It is important to note that both the formation and decomposition of H_2O_2 occur simultaneously during the photocatalytic process, as photogenerated charge carriers can consume H_2O_2. Consequently, the H_2O_2 production curves are fitted using a kinetic model that includes both a zero-order and a first-order term to evaluate the respective rates of H_2O_2 formation and decomposition. The kinetic equation, shown in eq 3, describes the changes in H_2O_2 concentration as a function of illumination time.[38,54]

$$[H_2O_2] = \frac{K_f}{K_d} \times \{1 - \exp(-K_d \times t)\} \quad (3)$$

Here, K_f (μM min^{-1}) and K_d (min^{-1}) represent the rate constants for H_2O_2 generation and decomposition, respectively, while $[H_2O_2]$ refers to the concentration of generated H_2O_2 (μM), and t denotes the reaction time (min).[55] In Figure S9b, the time-dependent H_2O_2 decomposition plot and kinetics plot in Figure 8b reveal that both 2D MoS_2 and $MnIn_2S_4$ exhibit higher decomposition rate constants (K_d of 0.01488 min^{-1} and 0.00482 min^{-1}, respectively) compared to the MS/MnIS-*x* heterostructure photocatalysts. The heterostructures with $MnIn_2S_4$ loadings ranging from 10 wt% to 40 wt% on 2D MoS_2 effectively suppress H_2O_2 decomposition. However, loadings beyond 40 wt%, such as 60 and 80 wt%, result in an increase in H_2O_2 decomposition. These photocatalytic results suggest that enhanced photogenerated charge separation and improved light absorption contribute to higher H_2O_2 formation while reducing decomposition.

The photocatalytic H_2O_2 production activity of the best catalyst (MS/MnIS40) was further evaluated at different pH levels (1.5, 3, 5, and 7). The pH-dependent experiments showed that the activity followed the trend: pH 3 > pH 1.5 > pH 5 > pH 7. At pH 3, a significantly enhanced H_2O_2 production rate of 606.7 μmol g^{-1} h^{-1} was achieved (Figure 8c), suggesting that protonation-induced ionic species contribute to the improved activity.[56] At a low pH of 1.5, the solution provides an excess of protons (H^+) in the reaction medium, which promotes the oxidation of H_2O_2 to water ($H_2O_2 + 2H^+ + 2e^- \rightarrow 2H_2O$), thereby reducing the overall H_2O_2 yield. Conversely, at pH 5 and 7, the lower availability of

https://doi.org/10.1021/acsaem.4c03296
ACS Appl. Energy Mater. 2025, 8, 3107−3119

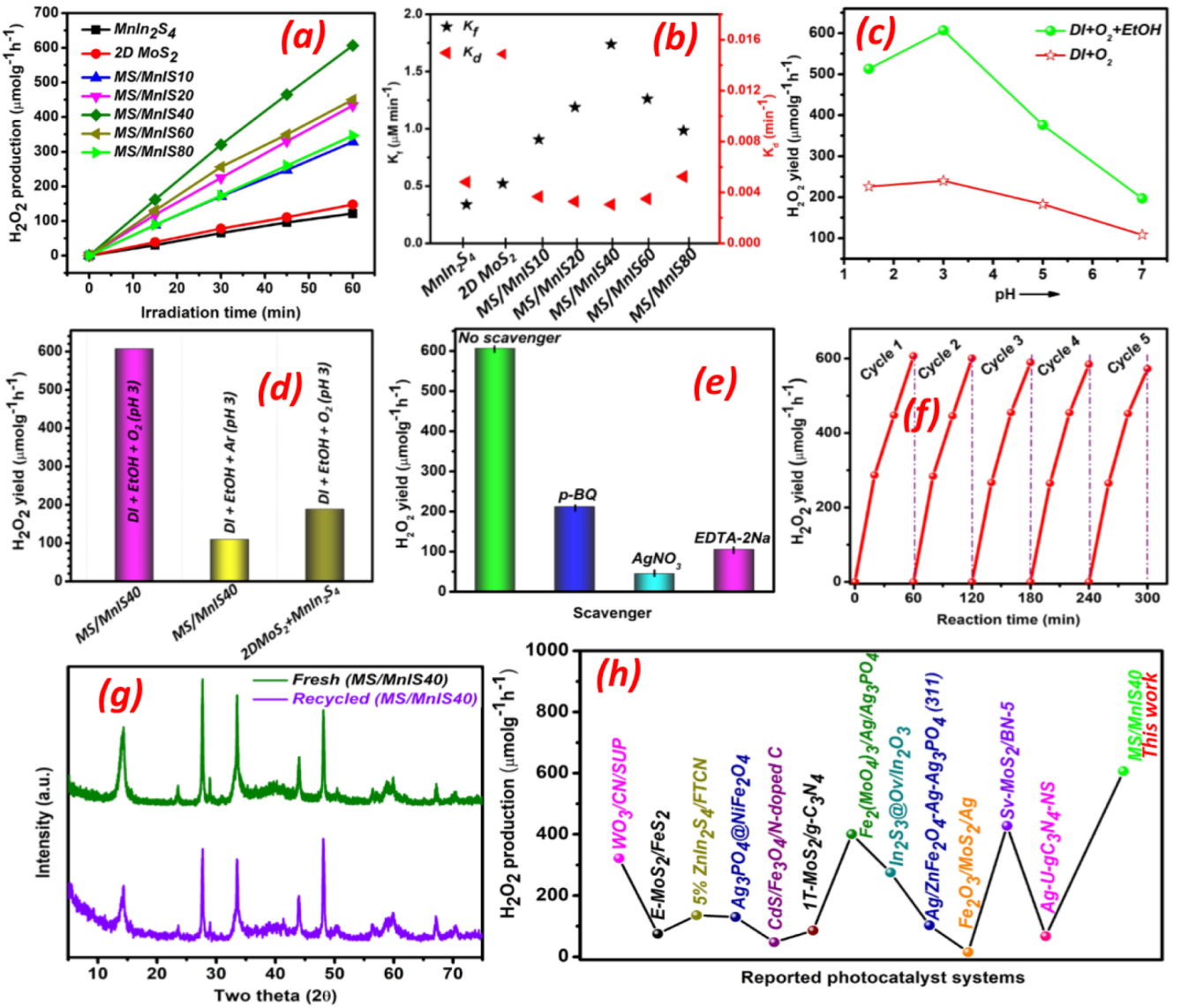

Figure 8. (a) The time-dependent plot of photocatalytic H_2O_2 production for various photocatalysts prepared in this study. (b) Kinetics plot of photocatalytic H_2O_2 decomposition on different photocatalysts. (c) H_2O_2 production at different pH levels using the optimal photocatalyst, MS/MnIS40. (d) H_2O_2 production under control conditions with MS/MnIS40. (e) H_2O_2 production with MS/MnIS40 in scavenger experiments. (f) Cycling experiments showing H_2O_2 production at different time intervals using MS/MnIS40. (g) XRD patterns of fresh and recycled MS/MnIS40 photocatalysts. (h) Comparison of photocatalytic H_2O_2 production with recently reported photocatalysts.

protons in the solution results in decreased H_2O_2 formation. Moreover, at a higher pH solution, $\bullet O_2^-$ becomes unstable, and H_2O_2 breaks down more quickly, further lowering its production. Hence, pH 3 was identified as the optimum pH for H_2O_2 production.[37,57,58]

To investigate the effect of the heterostructure in MS/MnIS40, control experiments using a physical blend of 60% 2D MoS_2 and 40% $MnIn_2S_4$ photocatalyst were conducted under optimal H_2O_2 production conditions (Figure 8d). Under these conditions, the H_2O_2 production rate was only 188.4 μmol g^{-1} h^{-1}, approximately 3.3 times lower than the best photocatalyst (MS/MnIS40). These results confirm that the proper formation of the heterostructure enhances visible light absorption and suppresses charge carrier recombination, leading to higher photocatalytic activity.

To gain further insight into the photocatalytic oxygen reduction reaction (ORR) pathway for H_2O_2 production by the MS/MnIS40 photocatalyst, control experiments with various scavengers were conducted. The photocatalytic performance of MS/MnIS40 was also evaluated under argon (Ar) atmosphere. When the reaction systems were purged with Ar, the H_2O_2 concentration dropped by 82%, demonstrating that O_2 plays a crucial role in the photocatalytic process, with H_2O_2 predominantly formed via the ORR. Interestingly, 18% of the H_2O_2 concentration was retained even under the Ar atmosphere, suggesting that the ORR process subsequently consumes the O_2 generated from water oxidation to produce H_2O_2 (Figure 8d). Two potential routes have been reported for synthesizing H_2O_2 from O_2 via a 2e$^-$ redox process: a two-step ORR process involving $^\bullet O_2^-$ as an intermediate species and a direct 2e$^-$ ORR process. To clarify the exact pathway, a $^\bullet O_2^-$ scavenger test was conducted using *p*-BQ. As shown in Figure 8e, the scavenger experiment with *p*-BQ indicated the formation of $\bullet O_2^-$ during the photocatalytic H_2O_2 production pathway, as adding *p*-BQ reduced H_2O_2 production by 65%. This result confirms that O_2 is reduced to form H_2O_2 through

https://doi.org/10.1021/acsaem.4c03296
ACS Appl. Energy Mater. 2025, 8, 3107−3119

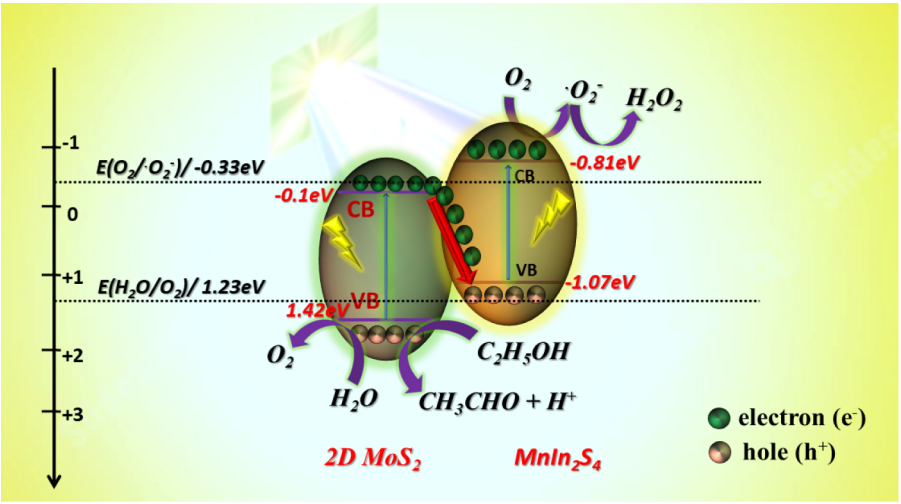

Figure 9. Possible mechanism of the photocatalytic H_2O_2 generation on 2D $MoS_2/MnIn_2S_4$ photocatalyst.

the $^{\bullet}O_2^-$ intermediate via a two-step process.[59] Further validation of $\bullet O_2^-$ involvement was conducted using the NBT test. As shown in Figure S10, NBT is selectively reduced by $\bullet O_2^-$, forming formazan. This reduction is evidenced by decreased NBT absorption intensity with prolonged illumination. The detailed experimental protocol of NBT experiments is provided in the Supporting Information. Furthermore, adding $AgNO_3$ confirmed that photogenerated electrons play a crucial role in the photocatalytic process, significantly reducing H_2O_2 production. Similarly, introducing EDTA-2Na as a hole (h^+) scavenger resulted in approximately a 76% reduction in H_2O_2 production compared to the case of no scavenger, highlighting the involvement of h^+ in the photocatalytic reaction. This result suggests that $\bullet O_2^-$ radicals, e^-, and h^+ play a major role in photocatalytic H_2O_2 production (Figure 8e).

The photostability of photocatalytic materials is a critical factor influencing H_2O_2 production efficiency. To evaluate this, the recyclability of the MS/MnIS40 photocatalyst for H_2O_2 production was tested over five cycles under identical experimental conditions. After each cycle, the photocatalyst was recovered by centrifugation, rinsed with ethanol, and dried at 60 °C for 5 h to assess its reusability. The dried photocatalyst was then reused in subsequent cycles. Figure 8f illustrates the H_2O_2 production activity of the MS/MnIS40 photocatalyst over five reuse cycles. After five cycles, the MS/MnIS40 heterostructure demonstrated remarkable stability, with H_2O_2 production remaining nearly unchanged and only a slight 7.8% decrease in H_2O_2 formation efficiency. This indicates that the heterostructure maintains its photocatalytic activity well, which is crucial for practical applications. Moreover, we performed XRD and XPS measurements of the recycled photocatalyst, as shown in Figures 8g and S11. The XRD patterns and XPS spectra of MS/MnIS40 before and after the fifth cycle of the photocatalytic reaction show no noticeable changes, indicating that the crystal structure and chemical states remained stable throughout the recycling process. These findings strongly confirm that the MS/MnIS40 heterostructure exhibits excellent photochemical stability and reusability, which is advantageous for long-term use and continuous operation in photocatalytic H_2O_2 production systems.

4.2. Photocatalytic Mechanism. The photocatalytic H_2O_2 production of as-prepared photocatalysts performance is presented in Figure 8a. Among them, MS/MnIS40 exhibits the highest photocatalytic activity compared to the other catalysts. Based on the experimental data, a photocatalytic H_2O_2 production mechanism is proposed, as illustrated in Figure 9. The combination of 2D MoS_2 and $MnIn_2S_4$ likely forms a Z-scheme heterojunction, as suggested by the Mott–Schottky and scavenger tests. Upon light irradiation of the MS/MnIS40 photocatalyst, photogenerated electrons accumulate in the CB of $MnIn_2S_4$, which has a more negative E_{CB} potential at −0.81 eV (vs V NHE), closely aligning with the reduction potential of O_2 at −0.33 eV (vs V NHE). The negative potential of $MnIn_2S_4$ CB and the $O_2/\bullet O_2^-$ couple facilitates rapid electron transfer, promoting the two-step one electron O_2 reduction necessary for H_2O_2 generation (eqs 4 and 5). The significant reduction in H_2O_2 yield in the presence of *p*-BQ, along with NBT experiments, confirms that $\bullet O_2^-$ is the primary active species. This suggests that H_2O_2 is produced through the further conversion of $\bullet O_2^-$ radicals, generated by the reduction of O_2 at −0.33 eV (vs V NHE). Simultaneously, the photogenerated holes in the VB of 2D MoS_2 oxidize water molecules, producing O_2 and H^+ (eq 6), as the VB potential of 2D MoS_2 (+1.42 V vs NHE) is more positive than the H_2O/O_2 potential (+1.23 V vs NHE). Control experiments under "Ar" purging showed that 18% of the H_2O_2 concentration was retained even in the absence of external O_2, suggesting that O_2 is generated from water oxidation. Moreover, the addition of ethanol significantly enhances H_2O_2 production by facilitating its activation, as photogenerated holes are efficiently consumed in the oxidation of ethanol. This reaction also provides H^+ ions, which later react with $\bullet O_2^-$ to form H_2O_2 (eq 7).[60] These factors are crucial for optimizing the photocatalytic ORR process to boost H_2O_2 production.

$$O_2 + e^- \rightarrow \bullet O_2^- \quad (4)$$

$$\bullet O_2^- + e^- + 2H^+ \rightarrow H_2O_2 \quad (5)$$

$$2H_2O + 2h^+ \rightarrow O_2 + 4H^+ + 2e^- \quad (6)$$

$$CH_3CH_2OH + 2h^+ \rightarrow CH_3CHO + 2H^+ \quad (7)$$

https://doi.org/10.1021/acsaem.4c03296
ACS Appl. Energy Mater. 2025, 8, 3107−3119

5. CONCLUSIONS

In conclusion, we have designed the ultrathin 2D MoS_2 nanosheets embedded with $MnIn_2S_4$ heterostructure photocatalysts for solar-driven H_2O_2 production using a facile two-step hydrothermal method. It was observed that the optimal loading of $MnIn_2S_4$ partially covers the 2D MoS_2 nanosheets, enhancing light absorption and providing more active sites. This leads to improved charge carrier separation and accelerated electron transfer, resulting in enhanced photocatalytic H_2O_2 production. However, excessive loading of $MnIn_2S_4$ covers the surface active sites of MoS_2 and blocks light absorption, leading to poor interfacial charge carrier separation and reduced photocatalytic activity. Moreover, the poor H_2O_2 production activity observed in physical blending experiments (2D MoS_2 + $MnIn_2S_4$) confirms that when proper heterostructures are formed, the MS/MnIS40 photocatalyst exhibits excellent H_2O_2 production activity, approximately 3.3 times higher than that of the physically blended mixtures. This demonstrates that the formation of an intimately connected/contacted heterostructure effectively inhibits charge recombination and accelerates charge transfer. The microscopy characterization results reveal a strong interfacial interaction between the components of 2D MoS_2 and $MnIn_2S_4$. The controlled radical trapping studies confirmed that H_2O_2 generation preferably occurred via a dual-step, one-electron O_2 reduction pathway. This study can inspire the exploration and development of effective noble-metal-free semiconductor heterostructure photocatalysts for solar-driven H_2O_2 generation.

■ ASSOCIATED CONTENT

Supporting Information

The Supporting Information is available free of charge at https://pubs.acs.org/doi/10.1021/acsaem.4c03296.

UV visible absorbance spectra of bulk MoS_2 and exfoliated MoS_2 nanosheets; images of exfoliated MoS_2 nanosheets dispersion; Tauc plot of bulk MoS_2 and MS/MnIS-*x* heterostructures photocatalyst; SEM elemental mapping of $MnIn_2S_4$; SEM images with corresponding elemental mapping of MS/MnIS60 and MS/MnIS80 heterostructure photocatalysts; HRTEM images of 2D MoS_2 nanosheets; TEM images of MS/MnIS40 photocatalysts; XPS survey spectra of $MnIn_2S_4$, 2D MoS_2, and MS/MnIS40; PL spectra of MS/MnIS10 and MS/MnIS80; Nyquist plot of pure $MnIn_2S_4$ MS/MnIS10 and MS/MnIS80 heterostructure photocatalysts; photocurrent studies of $MnIn_2S_4$, MS/MnIS10, and MS/MnIS80 photocatalysts; EIS equivalent fitting circuit and *Rs* and *Rct* value of 2D MoS_2, $MnIn_2S_4$, and MS/MnIS-*x* heterostructure photocatalysts; contact angle results of pristine $MnIn_2S_4$; photocatalytic H_2O_2 production rate at O_2 bubbled DI and water/EtOH mixture at pH 3; photocatalytic H_2O_2 decomposition at different time intervals; table showing the comparison of photocatalytic H_2O_2 production among recently reported other photocatalytic systems; NBT experiments on MS/MnIS40 photocatalyst; XPS spectra of recycled MS/MnIS40 photocatalyst (PDF)

■ AUTHOR INFORMATION

Corresponding Authors

Indrajit Sinha − *Department of Chemistry, Indian Institute of Technology (Banaras Hindu University), Varanasi 221005, India*; Email: isinha.apc@iitbhu.ac.in

Renzhi Ma − *Research Center for Materials Nanoarchitectonics (WPI-MANA), National Institute for Materials Science (NIMS), Tsukuba, Ibaraki 305-0044, Japan*; orcid.org/0000-0001-7126-2006; Email: MA.Renzhi@nims.go.jp

Authors

Uttam Kumar − *Research Center for Materials Nanoarchitectonics (WPI-MANA), National Institute for Materials Science (NIMS), Tsukuba, Ibaraki 305-0044, Japan; Department of Chemistry, Indian Institute of Technology (Banaras Hindu University), Varanasi 221005, India*; orcid.org/0000-0001-8327-8857

Emmanuel Picheau − *Research Center for Materials Nanoarchitectonics (WPI-MANA), National Institute for Materials Science (NIMS), Tsukuba, Ibaraki 305-0044, Japan*; orcid.org/0000-0002-6921-4555

Huanran Li − *Research Center for Materials Nanoarchitectonics (WPI-MANA), National Institute for Materials Science (NIMS), Tsukuba, Ibaraki 305-0044, Japan*

Zihan Zhang − *Research Center for Materials Nanoarchitectonics (WPI-MANA), National Institute for Materials Science (NIMS), Tsukuba, Ibaraki 305-0044, Japan*; orcid.org/0000-0002-4047-2278

Takayuki Kikuchi − *Research Center for Materials Nanoarchitectonics (WPI-MANA), National Institute for Materials Science (NIMS), Tsukuba, Ibaraki 305-0044, Japan*; orcid.org/0000-0003-0588-2172

Complete contact information is available at: https://pubs.acs.org/10.1021/acsaem.4c03296

Notes

The authors declare no competing financial interest.

■ ACKNOWLEDGMENTS

This research work was conducted under the International Cooperative Graduate Program (ICGP) of the National Institute for Materials Science (NIMS). Mr. Uttam Kumar gratefully acknowledges the support received from the IIT BHU Fellowship and the NIMS-ICGP internship program.

■ REFERENCES

(1) Yang, J.; Zeng, X.; Tebyetekerwa, M.; Wang, Z.; Bie, C.; Sun, X.; Marriam, I.; Zhang, X. Engineering 2D Photocatalysts for Solar Hydrogen Peroxide Production. *Adv. Energy Mater.* **2024**, *14* (23), 2400740.

(2) Gao, T.; Zhao, D.; Yuan, S.; Zheng, M.; Pu, X.; Tang, L.; Lei, Z. Energy Band Engineering of Graphitic Carbon Nitride for Photocatalytic Hydrogen Peroxide Production. *Carbon Energy* **2024**, *6* (11), No. e596.

(3) Khan, S.; Qaiser, M. A.; Qureshi, W. A.; Najeeb-Uz-Zaman Haider, S.; Yu, X.; Wang, W.; Liu, Q. Photocatalytic Hydrogen Peroxide Production: Advances, Mechanistic Insights, and Emerging Challenges. *J. Environ. Chem. Eng.* **2024**, *12* (5), 114143.

(4) Qiu, J.; Dai, D.; Yao, J. Tailoring Metal-Organic Frameworks for Photocatalytic H_2O_2 Production. *Coord. Chem. Rev.* **2024**, *501*, 215597.

(5) Kumar, U.; Sinha, I. Visible Light Photo-Fenton Degradation of p-Nitrophenol on Ag/Fe3O4/WO3 Nanocomposites: Experimental and Molecular Dynamics Investigations. *J. Environ. Chem. Eng.* **2023**, *11* (6), 111280.
(6) Kuntail, J.; Kumar, U.; Sinha, I. Insight into Photo-Fenton Reaction Mechanism on a Magnetite-GO Nanocomposite: Computational and Experimental Investigations. *Mol. Catal.* **2022**, *528*, 112491.
(7) Zheng, Y.; Zhou, H.; Zhou, B.; Mao, J.; Zhao, Y. Photocatalytic Production of H_2O_2 over Facet-Dependent Ti-MOF. *Catal. Sci. Technol.* **2022**, *12* (3), 969−975.
(8) Zuo, G.; Liu, S.; Wang, L.; Song, H.; Zong, P.; Hou, W.; Li, B.; Guo, Z.; Meng, X.; Du, Y.; Wang, T.; Roy, V. A. L. Finely Dispersed Au Nanoparticles on Graphitic Carbon Nitride as Highly Active Photocatalyst for Hydrogen Peroxide Production. *Catal. Commun.* **2019**, *123*, 69−72.
(9) Kumar, U.; Shrivastava, A.; Sinha, I. In Situ Use of Photocatalytically Produced H_2O_2 for Fenton Degradation of Organic Pollutants. *Catal. Sci. Technol.* **2024**, *14*, 2668.
(10) Ding, Y.; Maitra, S.; Halder, S.; Wang, C.; Zheng, R.; Barakat, T.; Roy, S.; Chen, L. H.; Su, B. L. Emerging Semiconductors and Metal-Organic-Compounds-Related Photocatalysts for Sustainable Hydrogen Peroxide Production. *Matter* **2022**, *5* (7), 2119−2167.
(11) Kondo, Y.; Kuwahara, Y.; Mori, K.; Yamashita, H. Design of Metal-Organic Framework Catalysts for Photocatalytic Hydrogen Peroxide Production. *Chem* **2022**, *8* (11), 2924−2938.
(12) Wang, L.; Zhang, J.; Zhang, Y.; Yu, H.; Qu, Y.; Yu, J. Inorganic Metal-Oxide Photocatalyst for H_2O_2 Production. *Small* **2022**, *18* (8), 2104561.
(13) Xie, L.; Wang, X.; Zhang, Z.; Ma, Y.; Du, T.; Wang, R.; Wang, J. Photosynthesis of Hydrogen Peroxide Based on g-C 3 N 4: The Road of a Cost-Effective Clean Fuel Production. *Small* **2023**, *19* (32), 2301007.
(14) Yan, J.; Li, Y.; Li, Y.; Ouyang, S.; Zhang, T. Recent Advances in Photocatalytic Hydrogen Peroxide Production, *PhotoMat (In Press)*, **2023**.
(15) Isaka, Y.; Oyama, K.; Yamada, Y.; Suenobu, T.; Fukuzumi, S. Photocatalytic Production of Hydrogen Peroxide from Water and Dioxygen Using Cyano-Bridged Polynuclear Transition Metal Complexes as Water Oxidation Catalysts. *Catal. Sci. Technol.* **2016**, *6* (3), 681−684.
(16) Song, H.; Wei, L.; Chen, C.; Wen, C.; Han, F. Photocatalytic Production of H_2O_2 and Its in Situ Utilization over Atomic-Scale Au Modified MoS_2 Nanosheets. *J. Catal.* **2019**, *376*, 198−208.
(17) Das, S.; Acharya, L.; Biswal, L.; Parida, K. Augmented Photocatalysis Induced by 1T-MoS2 Bridged 2D/2D $MgIn_2S_4$@1T/2H-MoS_2 Z-Scheme Heterojunction: Mechanistic Insights into H_2O_2 and H_2 Evolution. *Nanoscale Adv.* **2024**, *6* (3), 934−946.
(18) Mase, K.; Yoneda, M.; Yamada, Y.; Fukuzumi, S. Efficient Photocatalytic Production of Hydrogen Peroxide from Water and Dioxygen with Bismuth Vanadate and a Cobalt(II) Chlorin Complex. *ACS Energy Lett.* **2016**, *1* (5), 913−919.
(19) Zhang, Y.; Huang, H.; Wang, L.; Zhang, X.; Zhu, Z.; Wang, J.; Yu, W.; Zhang, Y. Cooperation of Congenital and Acquisitus Sulfur Vacancy for Excellent Photocatalytic Hydrogen Peroxide Evolution of CdS Nanorods from Air. *Chem. Eng. J.* **2023**, *454*, 140420.
(20) Yang, Y.; Wang, Q.; Zhang, X.; Deng, X.; Guan, Y.; Wu, M.; Liu, L.; Wu, J.; Yao, T.; Yin, Y. Photocatalytic Generation of H_2O_2 over a Z-Scheme Fe_2O_3@C@1T/2H-MoS_2 Heterostructured Catalyst for High-Performance Fenton Reaction. *J. Mater. Chem. A* **2023**, *11* (4), 1991−2001.
(21) Yang, Y.; Yu, H.; Wu, M.; Zhao, T.; Guan, Y.; Yang, D.; Zhu, Y.; Zhang, Y.; Ma, S.; Wu, J.; Liu, L.; Yao, T. Dual H_2O_2 Production Paths over Chemically Etched MoS_2/FeS_2 Heterojunction: Maximizing Self-Sufficient Heterogeneous Fenton Reaction Rate under the Neutral Condition. *Appl. Catal., B* **2023**, *325*, 122307.
(22) Li, Z.; Zhou, Z.; Ma, J.; Li, Y.; Peng, W.; Zhang, G.; Zhang, F.; Fan, X. Hierarchical Photocatalyst of In_2S_3 on Exfoliated MoS_2 Nanosheets for Enhanced Visible-Light-Driven Aza-Henry Reaction. *Appl. Catal., B* **2018**, *237*, 288−294.
(23) Kumar, U.; Das Chakraborty, S.; Sahu, R. K.; Bhattacharya, P.; Mishra, T. Improved Interfacial Charge Transfer on Noble Metal-Free Biomimetic CdS-Based Tertiary Heterostructure @ 2D MoS_2-CdS-Cu_2O with Enhanced Photocatalytic Water Splitting. *Adv. Mater. Interfaces* **2022**, *9* (2), 2101680.
(24) Kumar, U.; Sinha, I.; Mishra, T. Synthesis and Photocatalytic Evaluation of 2D MoS_2/TiO_2 Heterostructure Photocatalyst for Organic Pollutants Degradation. *Mater. Today: Proc.* **2024**, *112*, 66−72.
(25) Fang, Z.; Huang, X.; Wang, Y.; Feng, W.; Zhang, Y.; Weng, S.; Fu, X.; Liu, P. Dual-Defective Strategy Directing: In Situ Assembly for Effective Interfacial Contacts in MoS_2 Cocatalyst/In_2S_3 Light Harvester Layered Photocatalysts. *J. Mater. Chem. A* **2016**, *4* (36), 13980−13988.
(26) Zhao, H.; Fu, H.; Yang, X.; Xiong, S.; Han, D.; An, X. MoS_2/CdS Rod-like Nanocomposites as High-Performance Visible Light Photocatalyst for Water Splitting Photocatalytic Hydrogen Production. *Int. J. Hydrogen Energy* **2022**, *47* (13), 8247−8260.
(27) Kumar, D. P.; Hong, S.; Reddy, D. A.; Kim, T. K. Ultrathin MoS_2 Layers Anchored Exfoliated Reduced Graphene Oxide Nanosheet Hybrid as a Highly Efficient Cocatalyst for CdS Nanorods towards Enhanced Photocatalytic Hydrogen Production. *Appl. Catal., B* **2017**, *212*, 7−14.
(28) Reddy, D. A.; Park, H.; Ma, R.; Kumar, D. P.; Lim, M.; Kim, T. K. Heterostructured WS_2-MoS_2 Ultrathin Nanosheets Integrated on CdS Nanorods to Promote Charge Separation and Migration and Improve Solar-Driven Photocatalytic Hydrogen Evolution. *ChemSuschem* **2017**, *10* (7), 1563−1570.
(29) Zhao, M.; Guo, X.; Meng, Z.; Wang, Y.; Peng, Y.; Ma, Z. Ultrathin MoS_2 Nanosheet as Co-Catalyst Coupling on Graphitic g-C3N4 in Suspension System for Boosting Photocatalytic Activity under Visible-Light Irradiation. *Colloids Surf., A* **2021**, *631*, 127671.
(30) Liu, X.; Chen, X.; Xu, L.; Wu, B.; Tu, X.; Luo, X.; Yang, F.; Lin, J. Non-Noble Metal Ultrathin MoS_2 Nanosheets Modified $Mn_{0.2}Cd_{0.8}S$ Heterostructures for Efficient Photocatalytic H_2 Evolution with Visible Light Irradiation. *Int. J. Hydrogen Energy* **2020**, *45* (51), 26770−26784.
(31) Shen, S.; Zhao, L.; Zhou, Z.; Guo, L. Enhanced Photocatalytic Hydrogen Evolution over Cu-Doped ZnIn 2S4 under Visible Light Irradiation. *J. Phys. Chem. C* **2008**, *112* (41), 16148−16155.
(32) Zhang, B.; Shi, H.; Hu, X.; Wang, Y.; Liu, E.; Fan, J. A Novel S-Scheme MoS_2/$CdIn_2S_4$ Flower-like Heterojunctions with Enhanced Photocatalytic Degradation and H_2 Evolution Activity. *J. Phys. D: Appl. Phys.* **2020**, *53* (20), 205101.
(33) Chen, W.; He, Z.-C.; Huang, G.-B.; Wu, C.-L.; Chen, W.-F.; Liu, X.-H. Direct Z-Scheme 2D/2D $MnIn_2S_4$/g-C_3N_4 Architectures with Highly Efficient Photocatalytic Activities towards Treatment of Pharmaceutical Wastewater and Hydrogen Evolution. *Chem. Eng. J.* **2019**, *359*, 244−253.
(34) Song, Y.; Guo, Y.; Qi, S.; Zhang, K.; Yang, J.; Li, B.; Chen, J.; Zhao, Y.; Lou, Y. Cu_7S_4/$MnIn_2S_4$ Heterojunction for Efficient Photocatalytic Hydrogen Generation. *J. Alloys Compd.* **2021**, *884*, 161035.
(35) Dang, X.; Wu, S.; Zhao, H. Enhanced Photocatalytic Production of H_2O_2 through Regulation of Spatial Charge Transfer and Light Absorption over a $MnIn_2S_4$/WO_3(Yb, Tm) Z-Scheme System. *ACS Sustainable Chem. Eng.* **2022**, *10* (13), 4161−4172.
(36) Xie, J.; Zhang, H.; Li, S.; Wang, R.; Sun, X.; Zhou, M.; Zhou, J.; Lou, X. W.; Xie, Y. Defect-Rich MoS_2 Ultrathin Nanosheets with Additional Active Edge Sites for Enhanced Electrocatalytic Hydrogen Evolution. *Adv. Mater.* **2013**, *25* (40), 5807−5813.
(37) Kumar, U.; Shrivastava, A.; De, A. K.; Pai, M. R.; Sinha, I. Fenton Reaction by H_2O_2 Produced on a Magnetically Recyclable Ag/$CuWO_4$/$NiFe_2O_4$ Photocatalyst. *Catal. Sci. Technol.* **2023**, *13* (8), 2432−2446.
(38) Ahmed, M. T.; Abdullah, H.; Kuo, D. H. Photocatalytic H_2O_2 Generation over Microsphere Carbon-Assisted Hierarchical Indium

https://doi.org/10.1021/acsaem.4c03296
ACS Appl. Energy Mater. 2025, 8, 3107−3119

Sulfide Nanoflakes via a Two-Step One-Electron Pathway. *ACS Appl. Mater. Interfaces* **2023**, *15* (24), 29224−29235.
(39) Yu, W.; Zhu, Z.; Hu, C.; Lin, S.; Wang, Y.; Wang, C.; Tian, N.; Zhang, Y.; Huang, H. Point-to-Face Z-Scheme Junction $Cd_{0.6}Zn_{0.4}S$/g-C_3N_4 with a Robust Internal Electric Field for High-Efficiency H_2O_2 Production. *J. Mater. Chem. A* **2023**, *11* (12), 6384−6393.
(40) Shrivastava, A.; Kumar, U.; Sinha, I. Design and Development of the AgI/$NiFe_2O_4$ Photo-Fenton Photocatalyst. *Ind. Eng. Chem. Res.* **2024**, *63* (36), 15721−15734.
(41) Fang, Z.; Li, Y.; Li, J.; Shu, C.; Zhong, L.; Lu, S.; Mo, C.; Yang, M.; Yu, D. Capturing Visible Light in Low-Band-Gap C 4 N-Derived Responsive Bifunctional Air Electrodes for Solar Energy Conversion and Storage. *Angew. Chem.* **2021**, *133* (32), 17756−17762.
(42) Luo, N.; Chen, C.; Yang, D.; Hu, W.; Dong, F. S Defect-Rich Ultrathin 2D MoS_2: The Role of S Point-Defects and S Stripping-Defects in the Removal of Cr(VI) via Synergistic Adsorption and Photocatalysis. *Appl. Catal., B* **2021**, *299*, 120664.
(43) Tian, H.; Liu, M.; Zheng, W. Constructing 2D Graphitic Carbon Nitride Nanosheets/Layered MoS_2/Graphene Ternary Nanojunction with Enhanced Photocatalytic Activity. *Appl. Catal., B* **2018**, *225*, 468−476.
(44) Zhang, Z. Y.; Tian, H.; Jiao, H.; Wang, X.; Bian, L.; Liu, Y.; Khaorapapong, N.; Yamauchi, Y.; Wang, Z. L. SiO_2 Assisted Cu^0-Cu^+-NH_2 Composite Interfaces for Efficient CO_2 Electroreduction to C_{2+} Products. *J. Mater. Chem. A* **2024**, *12* (2), 1218−1232.
(45) Cheng, J.; Niu, Z.; Zhao, Z.; Pei, X.; Zhang, S.; Wang, H.; Li, D.; Guo, Z. Enhanced Ion/Electron Migration and Sodium Storage Driven by Different MoS_2-$ZnIn_2S_4$ Heterointerfaces. *Adv. Energy Mater.* **2023**, *13* (5), 2203248.
(46) Xi, T.-L.; Liu, L.-j.; Liu, Q.; Wang, H.-W.; Zuo, L.-Y.; Fan, H.-T.; Li, B.; Wang, L.-Y. Hollow MoS_2@$ZnIn_2S_4$ Nanoboxes for Improving Photocatalytic Hydrogen Evolution. *Int. J. Hydrogen Energy* **2024**, *62*, 62−70.
(47) Fang, Z.; Xia, Y.; Zhang, L.; Liu, J.; Li, J.; Hu, B.; Li, K.; Lu, Q.; Wang, L. Building the Confined CoS_2/MoS_2 Nanoreactor via Interface Electronic Reconfiguration to Synchronously Enhance Activity and Stability of Heterogeneous Fenton-like Reactions. *Appl. Catal., B* **2024**, *346*, 123769.
(48) Zhu, Z.; Huang, H.; Liu, L.; Chen, F.; Tian, N.; Zhang, Y.; Yu, H. Chemically Bonded α-Fe_2O_3/Bi_4MO_8Cl Dot-on-Plate Z-Scheme Junction with Strong Internal Electric Field for Selective Photo-Oxidation of Aromatic Alcohols. *Angew. Chem., Int. Ed.* **2022**, *61* (26), No. e202203519.
(49) Kumar, U.; Kuntail, J.; Kumar, A.; Prakash, R.; Pai, M. R.; Sinha, I. In-Situ H_2O_2 Production for Tetracycline Degradation on Ag/s-(Co_3O_4/$NiFe_2O_4$) Visible Light Magnetically Recyclable Photocatalyst. *Appl. Surf. Sci.* **2022**, *589*, 153013.
(50) Zhou, S.; Ma, W.; Kosari, M.; Lim, A. M. H.; Kozlov, S. M.; Zeng, H. C. Highly Active Single-Layer 2H-MoS_2 for CO_2 Hydrogenation to Methanol. *Appl. Catal., B* **2024**, *349*, 123870.
(51) Li, G.; Sun, J.; Hou, W.; Jiang, S.; Huang, Y.; Geng, J. Three-dimensional porous carbon composites containing high sulfur nanoparticle content for high-performance lithium−sulfur batteries. *Nat. Commun.* **2016**, *7* (1), 10601.
(52) Tian, H.; Zhang, Z. Y.; Fang, H.; Jiao, H.; Gao, T. T.; Yang, J. T.; Bian, L.; Wang, Z. L. Selective Electrooxidation of Methane to Formic Acid by Atomically Dispersed CuOx and Its Induced Lewis Acid Sites on V_2O_5 in a Tubular Electrode. *Appl. Catal., B* **2024**, *351*, 124001.
(53) Sebastia-Saez, D.; Gu, S.; Ramaioli, M. Effect of the Contact Angle on the Morphology, Residence Time Distribution and Mass Transfer into Liquid Rivulets: A CFD Study. *Chem. Eng. Sci.* **2018**, *176*, 356−366.
(54) Zhang, X.; Yu, J.; Macyk, W.; Wageh, S.; Al-Ghamdi, A. A.; Wang, L. C3N4/PDA S-Scheme Heterojunction with Enhanced Photocatalytic H_2O_2 Production Performance and Its Mechanism. *Adv. Sustain. Syst.* **2023**, *7* (1), 2200113.
(55) Yang, Y. Y.; Guo, H.; Huang, D. W.; Li, L.; Liu, H. Y.; Sui, L.; Wu, Q.; Zhu, J. J.; Zhang, L.; Niu, C. G. Simultaneously Tuning Oxygen Reduction Pathway and Charge Transfer Dynamics toward Sacrificial Agent-Free Photocatalytic H_2O_2 Production for in-Situ Water Disinfection. *Chem. Eng. J.* **2024**, *479*, 147863.
(56) Wang, S.; Xie, Z.; Zhu, D.; Fu, S.; Wu, Y.; Yu, H.; Lu, C.; Zhou, P.; Bonn, M.; Wang, H. I.; Liao, Q.; Xu, H.; Chen, X.; Gu, C. Efficient Photocatalytic Production of Hydrogen Peroxide Using Dispersible and Photoactive Porous Polymers. *Nat. Commun.* **2023**, *14* (1), 6891.
(57) Li, R.; Zhang, D.; Shi, Y.; Li, C.; Long, Y.; Yang, M. Developing a Built-in Electric Field in CdS Nanorods by Modified MoS_2 for Highly Efficient Photocatalytic H_2O_2 Production. *J. Catal.* **2022**, *416*, 322−331.
(58) Wang, J.; Yang, L.; Zhang, L. Constructed 3D Hierarchical Micro-Flowers $CoWO_4$@Bi_2WO_6 Z-Scheme Heterojunction Catalyzer: Two-Channel Photocatalytic H_2O_2 Production and Antibiotics Degradation. *Chem. Eng. J.* **2021**, *420*, 127639.
(59) Wang, F.; Yue, S.; Han, X.; Zhang, T.; Han, A.; Wang, L.; Liu, J. ZnS/C Dual-Quantum-Dots Heterostructural Nanofibers for High-Performance Photocatalytic H_2O_2 Production. *ACS Appl. Mater. Interfaces* **2024**, *16* (2), 2606−2613.
(60) Ma, L.; Gao, Y.; Wei, B.; Huang, L.; Zhang, N.; Weng, Q.; Zhang, L.; Liu, S. F.; Jiang, R. Visible-Light Photocatalytic H_2O_2 Production Boosted by Frustrated Lewis Pairs in Defected Polymeric Carbon Nitride Nanosheets. *ACS Catal.* **2024**, *14* (4), 2775−2786.

https://doi.org/10.1021/acsaem.4c03296
ACS Appl. Energy Mater. 2025, 8, 3107−3119